Through-thickness permeability study of orthogonal and angle-interlock woven fabrics

Abstract:

Three-dimensional (3D) woven textiles, including orthogonal and angle-interlock woven fabrics, exhibit high inter-laminar strength in addition to good in-plane mechanical properties and are particularly suitable for lightweight structural applications. Resin Transfer Moulding (RTM) is a cost-effective manufacturing process for composites with 3D woven reinforcement. With increasing preform thickness, the influence of through-thickness permeability on RTM processing of composites becomes increasingly significant. This study proposes an analytical model for prediction of the through-thickness permeability, based on Poiseuille's law for hydraulic ducts approximating realistic flow channel geometries in woven fabrics. The model is applied to four 3D-woven fabrics and three 2D woven fabrics. The geometrical parameters of the fabrics were characterized employing optical microscopy. For validation, the through–thickness permeability was determined experimentally. The equivalent permeability of inter-yarn gaps was found to account for approximately 90 % of the through-thickness permeability for the analysed fabrics. The analytical predictions agree well with the experimental data of the seven fabrics.

Keywords: 3D-woven fabric, through-thickness permeability, analytical model

1 Introduction

Because of their high specific stiffness and high specific strength, polymer composites have found use in the aerospace, nautical, automotive and sports equipment industries [1-3], where they replace other materials, in particular metals. In the aeronautic and automotive industries, lightweight composite structures have become important in the development of sustainable fuel-efficient transport solutions [4]. Demand for cost-effective manufacture of high-performance composite structures with woven textile reinforcements has driven research into Liquid Composite Moulding (LCM) processes. A key research topic is characterization of the reinforcement permeability tensor, which determines the impregnation of the reinforcement with liquid resin in LCM [5-8]. Quantifying the permeability accurately and reliably remains a major challenge, because resin flow paths within deformable textile reinforcements are inherently geometrically complex and variable.

The permeability of porous media is defined by Darcy's law [9], which describes a linear relationship between flow velocity, V, and pressure drop, ΔP, in uni-directional flow over the length of the porous medium, L:

$$V = -\frac{K}{\mu}\frac{\Delta P}{L}\ , \qquad (1)$$

Here, μ is the fluid viscosity, and K is the permeability of the medium. In a three-dimensional case, $[K]$ is a symmetrical 3x3 tensor with components $K_{xy} = K_{yx},\ K_{xz} = K_{zx},\ K_{yz} = K_{zy}$. $[K]$ can be transformed to $[\overline{K}]$ such that:

$$[\bar{K}] = \begin{bmatrix} K_{xx} & 0 & 0 \\ 0 & K_{yy} & 0 \\ 0 & 0 & K_{zz} \end{bmatrix} . \qquad (2)$$

Here, K_{xx}, K_{yy} and K_{zz} are the principal permeabilities.

Woven fabrics are dual-scale porous media and generally exhibit different permeability in different material directions, i.e. the values of the two in-plane permeabilities, K_{xx} and K_{yy}, and the through-thickness permeability, K_{zz}, are different. The in-plane permeability of multi-layered textile preforms was investigated, for instance, by Mogavero and Advani [10], who compared experimental data with permeability predictions based on thickness-weighted averaging of layer permeabilities:

$$K_{xx\ or\ yy} = \frac{1}{L}\sum_{i=1}^{N} l_i K_i \quad . \qquad (3)$$

Here, K_i is the value of K_{xx} or K_{yy} of fabric layer i, l_i is the thickness of the fabric layer, and L is the thickness of the entire preform. The model gave a reasonable estimate with deviations from experimental data between 14.2 % and 23.8 %. For K_{zz} of 3D woven fabrics, Endruweit and Long [11] developed the semi-empirical relation:

$$K_{zz} = \frac{M\pi k^2 n^2 {R_f}^4 \sin\alpha}{4} \quad . \qquad (4)$$

Here, M is the number of binder yarns per fabric surface area, k a form factor, n is the filament count of the binder yarns, R_f is the filament radius, and α is the angle between the axis of the binder yarns and the fabric plane. Eq. 4 cannot predict K_{zz} directly since the parameter k for a particular fabric needs to be determined from experiments.

In the present study, an analytical model is derived from a generalized Poiseuille's law for predicting K_{zz} of 3D woven fabrics based purely on geometrical information on the fabric architectures. For orthogonal and angle-interlock 3D woven reinforcement fabrics, the model was validated with the experimental permeability data. For comparison, plain and twill weave 2D fabrics were analysed.

Orthogonal and angle-interlock fabrics have architectures with alternating uni-directional layers of non-crimp warp and weft yarns. In orthogonal weave fabrics, binder yarns are oriented in the through-thickness direction, while in angle-interlock fabrics, binder yarns are oriented at an angle to the fabric plane (Fig. 1a and b). On the other hand, 2D fabrics consist of one layer each of warp and weft

yarns. For the example of plain weave fabrics, each weft yarn crosses over a warp yarn, then under the next warp yarn, and so on. In a twill weave fabric, each weft yarn crosses over a number of warp yarns, u, then crosses under a number of warp yarns, b, thus forming a distinctive diagonal pattern. Hence, twill weave patterns are designated by a fraction, u/b. Analytical prediction of the through-thickness permeability requires geometrical characterization of flow channels formed in the respective fabric structure. While X-ray micro-Computed Tomography (μ-CT) can be used for scanning the internal architecture of 3D materials [12-15], as illustrated in Figure 1c and d, data used for permeability prediction were obtained using optical microscopy.

2 Theoretical analysis of K_{zz}

2.1 Orthogonal and angle-interlock woven fabrics

Here, a 3D woven fabric, either orthogonal or angle-interlock, is assumed to comprise a number of identical sub-layers. Each sub-layer is formed from one layer of warp yarns and one layer of weft yarns.. Since there is always one more weft layer than warp layer (Fig. 1a), the number of sub-layers is N+1/2. Since the ½ sub-layer only contains yarns aligned in one direction, the gap space is assumed to be large compared to a full (bi-directional) sub-layer, and its influence on the through-thickness permeability of the fabric is neglected. A homogenization approach [10, 17] was used to simplify the 3D woven structure, as shown in Fig. 2, where i is an arbitrary sub-layer, while N is the total number of sub-layers. For laminar through-thickness flow of a Newtonian fluid through the fabric, the fluid is assumed to penetrate the sub-layers successively. According to Eq. 1, a linear relationship between $\Delta P/L$ and V applies to an arbitrary sub-layer of the 3D woven fabric:

$$\frac{\Delta P_i}{l_i} = -\frac{\mu}{K_i} V \qquad (5)$$

The total pressure drop, $\Delta P = \sum_{i=1}^{N} \Delta P_i$, and thickness, $L = \sum_{i=1}^{N} l_i$, determine the value of K_{zz} of the 3D woven fabric based on Eq. 1:

$$\sum_{i=1}^{N} \Delta P_i = -\frac{\mu V}{K_{zz}} \sum_{i=1}^{N} l_i \qquad (6)$$

Since the equation of continuity applies, the value of V is identical for each fabric sub-layer. Thus,

$$\Delta P = \sum_{i=1}^{N} \Delta P_i = -\mu V \sum_{i=1}^{N} \frac{l_i}{K_i} \qquad (7)$$

Eqs. 6 and 7 give an approximation for K_{zz} of a 3D woven fabric on the basis of sub-layer fabric permeabilities, K_i, thicknesses, l_i, and the thickness of the whole 3D woven fabric, L:

$$K_{zz} = \frac{L}{\sum_{i=1}^{N} \frac{l_i}{K_i}} \quad (8)$$

2.2 Sub-layer of 3D woven fabrics

Unit cells of an orthogonal 3D woven fabric and a plain weave fabric are shown schematically in Fig. 3c and e. The through-thickness permeability, K_f, of a unit-cell depends on the yarn permeability, K_y, and equivalent permeability of inter-yarn gaps , K_g. While K_y depends on filament radius, R_f, and yarn fibre volume fraction, V_f, [18-22] K_g is determined by the in-plane gap dimensions and their change through the thickness.

In a fabric unit-cell, Q_g is the volumetric flow rate through the inter-yarn gap with cross-sectional area A_g; Q_y and Q_f, and A_y and A_f are the corresponding parameters for yarns and the fabric. According to Eq. 1, the relationship between K_y, K_g and K_f is:

$$Q_f = \frac{-A_f K_f}{\mu} \frac{\Delta P}{L} \quad (9)$$

$$Q_f = Q_g + Q_y \quad (10)$$

$$\frac{-A_f K_f}{\mu} \frac{\Delta P}{L} = \frac{-A_g K_g}{\mu} \frac{\Delta P}{L} + \frac{-A_y K_y}{\mu} \frac{\Delta P}{L} \quad (11)$$

If the area coverage in a fabric sub-layer is $\Phi = A_g / A_f$, Eq. 11 can be expressed as:

$$K_f = \Phi K_g + (1 - \Phi) K_y \quad (12)$$

which describes the permeability for a sub-layer of a 3D woven fabric.

Figure 4 shows the fabric permeability and the contributions of equivalent gap permeability and yarn permeability as expressed in Eq. 12 as functions of Φ, assuming a constant value of K_y. If a fabric has a high yarn packing density, where inter-yarn gaps disappear (Φ = 0), K_f is equivalent to K_y. As Φ increases, the contribution of K_y to K_f decreases linearly while K_g increases significantly. A critical size of inter-yarn gap exists, where $(1 - \Phi)K_y$ equals ΦK_g, i.e. the two dashed curves in Fig. 4 cross, and K_y and K_g contribute equally to K_f. The dependence of K_g and K_y on fabric geometrical parameters, as indicated in Fig. 3c and d, will be discussed in the following.

Introducing some simplifications of the unit cell geometry (neglecting crimp if present, assuming straight warp and weft yarns with constant cross-section, assuming rectangular cross-section of the binder yarn), the actual gap cross-section (Fig. 3) can be characterized by the hydraulic radius [22-24]:

$$R = \frac{(S_w - D_w)(S_j - D_j) - B_w \cdot B_j}{2(S_w - D_w - B_w + S_j - D_j - B_j)} \quad (13)$$

where S_j, D_j and B_j are the measured spacing and width of warp yarns and height of binder yarns, while S_w, D_w and B_w are the measured spacing and widths of weft yarns and width of binder yarns, respectively. While R is the hydraulic radius at the narrowest flow channel cross-section,

$$a = \frac{S_j S_w}{2(S_j+S_w)} - R \qquad (14)$$

is the distance from the narrowest flow channel boundary to the boundary of the unit-cell. A parabolic equation is used to approximate the yarn cross-section through-thickness with the coordinates in through-thickness direction, x, and in-plane, r, shown in Fig. 3d:

$$r = R + \frac{x^2}{\lambda a} \qquad (15)$$

Here, the parameter, λ, is related to the yarn height and determines the curvature of the channel geometry. The smaller the value of λ, the sharper the tip of the yarn cross-section. The exact flow channel geometry can be obtained from microscopic images of cross-sections of warp and weft yarns, where coordinates can be measured using image analysis software and approximated by a second-order polynomial using least-squares analysis [22]. This allows the value of λ in Eq. 15 to be determined directly.

Flow though a gap with varying cross-section is analysed based on the Hagen-Poiseuille equation [25], assuming that at each position through-thickness the gap can be treated as a long straight tube:

$$\int_{P_2}^{P_1} dP = \frac{8c\mu Q}{\pi} \int_{-\frac{l_i}{2}}^{\frac{l_i}{2}} \frac{dx}{(R+\frac{x^2}{\lambda a})^4} \qquad (16)$$

Here c is a laminar friction constant for conversion of a duct with rectangular cross-section (with aspect ratio α=width/length) to a virtual circular duct with identical equivalent permeability, where α can be determined from microscopic images as shown in Fig. 3e. The derivation of c can be found in the appendix. Integration of Eq. 16 gives:

$$\Delta P = \frac{8c\mu Q}{\pi} \frac{\sqrt{\lambda a R}}{R^4} \left\{ \frac{5}{8} \tan^{-1}\left(\frac{l_i}{2\sqrt{\lambda a R}}\right) + \frac{\frac{l_i}{2\sqrt{\lambda a R}}\left[15\left(\frac{{l_i}^2}{4\lambda a R}\right)^2 + \frac{40{l_i}^2}{4\lambda a R} + 33\right]}{24\left(\frac{{l_i}^2}{4\lambda a R}+1\right)^3} \right\} \qquad (17)$$

From Eqs. 1 and 17, K_g can be obtained as follows:

$$K_g = \frac{l_i \cdot R^2}{8c\sqrt{\lambda a R} \cdot \left\{ \frac{5}{8} \tan^{-1}\left(\frac{l_i}{2\sqrt{\lambda a R}}\right) + \frac{\frac{l_i}{2\sqrt{\lambda a R}}\left[15\left(\frac{{l_i}^2}{4\lambda a R}\right)^2 + \frac{40{l_i}^2}{4\lambda a R} + 33\right]}{24\left(\frac{{l_i}^2}{4\lambda a R}+1\right)^3} \right\}} \qquad (18)$$

If crimp is introduced, as in unit cells of 2D woven fabrics, determining K_y is more complicated because the yarn orientation relative to the flow direction varies for different weave architectures. While Gebart [18] analyzed fluid flow along and perpendicular to parallel filaments with ideal periodic arrangement (i.e. in yarns), Advani et al. [26] summarized the theory of flow in anisotropic materials with an angle, θ, relative to the main flow direction. Combination of the two models gives an expression for K_y for undulated yarns with crimp angle, θ, in a plain weave fabric:

$$K_y^1 = \frac{8{R_f}^2}{53}\frac{(1-V_f)^3}{V_f^2}\cos^2\theta + \frac{16{R_f}^2}{9\sqrt{6}\pi}\left(\sqrt{\frac{V_{fmax}}{V_f}}-1\right)^{5/2}\sin^2\theta - \frac{\sin^2\theta\cos^2\theta\left(\frac{16{R_f}^2}{9\sqrt{6}\pi}\left(\sqrt{\frac{V_{fmax}}{V_f}}-1\right)^{5/2}-\frac{8{R_f}^2(1-V_f)^3}{53\quad V_f^2}\right)^2}{\frac{8{R_f}^2(1-V_f)^3}{53\quad V_f^2}\sin^2\theta+\frac{16{R_f}^2}{9\sqrt{6}\pi}\left(\sqrt{\frac{V_{fmax}}{V_f}}-1\right)^{5/2}\cos^2\theta}$$

(19-1)

For a twill weave fabric characterized by u/b, there are $(u+b-1)/(u+b)$ flat yarn segments and $1/(u+b)$ segments of yarns inclined at a crimp angle, θ. Hence the total contribution of a yarn to the through-thickness fabric permeability can be described as:

$$K_y^2 = \frac{(u+b-1)}{(u+b)}\cdot\frac{16{R_f}^2}{9\sqrt{6}\pi}\left(\sqrt{\frac{V_{fmax}}{V_f}}-1\right)^{\frac{5}{2}} + \frac{K_y^1}{(u+b)} \qquad (19\text{-}2)$$

Here, V_f is the fibre volume fraction in a yarn; V_{fmax} is the maximum fibre volume fraction, which is achieved when the filaments are in contact with each other. The value of V_{fmax} is $\pi/4$ for square filament arrangements and $\pi/2\sqrt{3}$ for hexagonal filament arrangements [18]. The effect of low level yarn twist (Fig. 6a) on K_y is ignored here. For unit cells of 3D woven fabrics as shown in Fig. 3c, K_y is determined by fluid flow along filaments in binder yarns, and flow perpendicular to filaments in warp and weft yarns. Hence, from Gebart's model and Eq. 11 for ratios of cross-sectional areas:

$$K_y^3 = \frac{S_j\cdot S_w-(S_j-D_j)\cdot(S_w-D_w)}{S_j\cdot S_w}\cdot\frac{16{R_f}^2}{9\sqrt{6}\pi}\left(\sqrt{\frac{V_{fmax}}{V_f}}-1\right)^{\frac{5}{2}} + \frac{B_j\cdot B_w}{S_j\cdot S_w}\cdot\frac{8{R_f}^2}{53}\frac{(1-V_f)^3}{V_f^2} \qquad (20)$$

In Eqs. 19 and 20, yarn permeabilities are derived assuming hexagonal fibre arrangement. For a square fibre arrangement, the constants (53 and $9\sqrt{6}$) would need to be replaced with 57 and $9\sqrt{2}$.

3 Experimental study of K_{zz}

The equations for the permeabilities of sub-layers, K_f, and entire fabrics, K_{zz}, were applied to four 3D woven carbon fibre reinforcement fabrics (two orthogonal and two angle-interlock fabrics) and validated based on experimental permeability data.

Fabric 'A' is an angle-interlock 3D woven fabric, comprising three layers of weft yarns with lenticular cross-section two layers of warp yarns and binder yarns, both with rectangular cross-section. Fabric 'O' is an orthogonal 3D woven fabric with six layers of warp yarns, seven layers weft yarns and binder yarns with approximately rectangular cross-section. The real internal geometry of the two 3D woven fabrics was characterized based on micrographs of composite specimens [11]. In Table 1, N' is the number of layers of 3D woven fabric, V_F is the fibre volume fraction in the fabric, i.e. the total fibre volume divided by the volume occupied by the fabric.

The through-thickness permeability was measured in a saturated uni-directional flow experiments. In a stiff cylindrical flow channel with a liquid inlet at the bottom and a liquid outlet on top (inner diameter 80 mm), fabric specimens are held in position by stiff perforated plates, which allow parallel flow perpendicular to the fabric plane. The distance between the perforated plates is given by the height of spacer rings. Engine oil with known viscosity-temperature characteristics ($\mu \approx 0.3\text{Pa} \cdot \text{s}$ at 20 ºC) was used as a test fluid. The flow rate is set on a gear pump and monitored using a flow meter. Pressure transducers are mounted on both sides of the fabric specimen for measurement of the pressure drop [11]. The value of K_{zz} was calculated according to Eq. 1 with the constant flow rate (laminar flow with small Reynolds numbers) and measured pressure drop. Each test was repeated three times with a fresh sample.

In addition, three 2D technical textiles (cotton or cotton/polyester) were analysed. Measured geometrical fabric parameters are listed in Table 2. Top view and side view images of 2D fabrics were acquired using an optical microscope. The images were used to measure the yarn spacing, S_x, from the distance between centrelines of two neighboring parallel yarns, yarn widths and heights, D_x and B_x, from fabric cross sectional dimensions, and the values of R_f, λ and V_f. The fabric thickness, L, was tested using the Kawabata Evaluation System (KES-F) at an applied normal pressure of 0.05 kPa.

The through-thickness permeability of 2D fabrics was measured according to BS EN ISO 9237:1995. The apparatus for the experiment is an air permeability tester FX 3300. While the fabric is clamped in position, a suction fan forces air to flow perpendicularly through the fabric. The volumetric flow rate is measured and divided by the specimen area to give the velocity of air flow. The pressure drop in the experiment for all fabrics is set to 500 Pa, with an accuracy of at least 2 %. Using the measured velocity, pressure drop and fabric thickness, permeability is calculated according to Darcy's law.

4 Results and discussions

Figure 5a shows the surface morphology and cross-sections of three 2D woven fabrics. Inter-yarn gaps

can be identified more clearly for the plain weave fabric, P_1, than for the twill weave fabrics, T_1 and T_2, either based on top or side views of the fabrics. The yarns in these 2D fabrics have 'Z'- twist, which results in dense filament packing in the yarns and low values of K_y. Since the level of yarn twist is low, Eq. 19 is suitable to approximate K_y assuming aligned and parallel filaments.

The cross-sections in Fig. 5b, illustrate the internal geometry of orthogonal and angle-interlock woven fabrics. The warp and weft yarns in the orthogonal 3D woven fabric are straight and parallel. Binder yarns follow paths through the fabric thickness, fixating warp and weft yarns and generating inter-yarn gaps to form flow channels. In the angle-interlock woven fabric, binder yarns follow paths resembling sine/cosine curves through the layers of warp and weft yarns. The cross-section normal to the weft direction shows an offset between layers of weft yarns by half a yarn width, which needs to be considered for definition of the angle-interlock fabric unit cell. The white rectangular frames in the top views of the fabrics illustrate the fabric unit cell areas. Measuring the geometrical dimensions of each fabric unit cell allows the sub-layer permeability, K_f, and the permeability of the entire fabric, K_{zz}, to be predicted.

Table 3 gives measured values of α for the seven woven fabrics based on the measured yarn spacing and width in Tables 1 and 2. The value of c decreases with increasing value of α. Additional values for α are listed as reference for fabrics with different weave densities and porosities. Table 4 quantifies the contributions of K_g and K_y to K_f for 2D woven fabrics based on the measured dimensions and Eqs. 12, 18 and 19. The contribution of K_y to K_f is less than 12 % if Φ is greater than 1 %, indicating the significant effect of K_g on K_f. For fabric P_1, K_f is greater than for fabrics T_1 and T_2, owing to the greater value of Φ. Fabrics T_1 and T_2 show similar values of K_f since the values of Φ are similar. This implies that for most 2D woven fabrics, K_{zz} can be estimated merely considering K_g and Φ, and Eq. 19 only needs to be applied for fabrics with dense yarn packing. Figure 6 compares predicted (Eqs. 8 and 12) and measured values of K_{zz} for the seven woven fabrics. The comparison suggests that characterizing the internal structure of a fabric accurately and considering flow through an inter-yarn gap with varying cross-section (Fig. 3d) when determining the value of K_g (Eq. 18),, allows accurate prediction of K_f for 2D fabrics or a sub-layer of a 3D woven fabric.

The predicted value of K_{zz} for orthogonal and angle-interlock 3D woven fabrics was based on Eqs. 8, 12, 18 and 20. The geometrical parameters and fabric specifications for the prediction were taken from Table 1. Fabric 'A' shows relatively wide gaps between adjacent parallel yarns and high K_{zz} values owing to the small values of V_F and high values of K_i. For V_F = 0.41 (A_1), the predicted value of K_{zz}, 28.9×10^{-12} m^2, is similar to the measured average value, 23.5×10^{-12} m^2, indicating a relative difference of 23.3 %. For V_F = 0.47 (A_2), the prediction shows very good agreement with experimental data. Comparisons for fabric 'O' give similar result. For V_F = 0.55 (O_1), the measured K_{zz} is 10.3×10^{-12} m^2 whereas the prediction is 12.9×10^{-12} m^2. All predicted peremabilities for the 3D woven fabrics lie within

the range defined by the standard deviations of the experimental data. As expected, Fig. 6 shows that K_{zz} decreases with increasing V_F due to the reduction of overall gap space in the fabric.

5 Conclusions

The though-thickness permeability of orthogonal and angle-interlock 3D woven fabrics was studied analytically. It is determined by the height and through-thickness permeability of each sub-layer, the number of sub-layers, and the entire fabric thickness. The through-thickness permeability of each sub-layer depends on the yarn permeability in the flow direction, the equivalent permeability of inter-yarn gaps and the areal coverage of the fabric. The yarn permeability was modeled by combining axial and transverse permeabilities based on the local yarn crimp angle. The equivalent gap permeability was modelled based on conversion of the actual gap cross-section to a circular cross-section and varying the cross-section through the fabric thickness according to measured yarn cross-sectional profiles. For seven woven fabrics of different architectures, geometrical fabric parameters were characterized in detail by optical microscopy. Calculation of yarn permeability, equivalent gap permeability, and fabric permeability shows that the equivalent gap permeability dominates the fabric permeability, even if the areal coverage of inter-yarn gaps is only around 1 %. Comparison of predicted and measured values of the through-thickness permeability of orthogonal and angle-interlock woven fabrics shows close agreement for each sample, indicating good accuracy of the permeability models. Studies on the sensitivity of the fabric through-thickness permeability to variation of the geometrical parameters and extension of the theoretical analysis to 3D woven fabrics with different architecture are ongoing.

Acknowledgements

The work was supported in part by the projects: RGC No.: 5158/13E and NSFC funding Grant No. 51373147 and Project code: JC201104210132A.

Appendix

The frictional pressure loss in flow along a duct with arbitrary cross section, e.g., the duct formed by interwoven yarns, is usually expressed in terms of a friction factor ξ (also called a resistance coefficient) which is defined as [27]:

$$\xi = \frac{\Delta P}{L} \cdot \frac{2D_h}{\rho V^2} \qquad \text{(a1)}$$

where ΔP and L are the pressure loss and the length of flow channel, D_h is the hydraulic diameter as defined below, ρ is the density of the fluid, and V is the mean velocity over the duct cross section. The hydraulic diameter is defined as four times the duct cross-sectional area A' divided by the wetted

perimeter *O*:

$$D_h = 4A'/O \qquad \text{(a2)}$$

For a circular tube, D_h is equivalent to its geometrical diameter. The friction factor can be derived analytically for many cross sections (circular, triangular, quadratic, etc.) in laminar flows [18,28] and can be expressed as:

$$\xi = c' \cdot \frac{\mu}{\rho V D_h} \qquad \text{(a3)}$$

where *c'* is a dimensionless shape factor and μ is the fluid viscosity. Then Eqs. a1 and a3 give:

$$\frac{\Delta P}{L} = c' \cdot \frac{\mu V}{2{D_h}^2} \qquad \text{(a4)}$$

Comparing Eq. 1 with Eq. a4 gives:

$$\mathrm{K} = \frac{2{D_h}^2}{c'} \qquad \text{(a5)}$$

The Hagen–Poiseuille equation describes a laminar fluid flow along a circular tube (diameter D_h), which has a relationship of pressure gradient and flow velocity:

$$\frac{\Delta P}{L} = \frac{32\mu V}{{D_h}^2} \qquad \text{(a6)}$$

Comparison of Eqs. a6 and 1 gives the equivalent permeability of a circular tube:

$$\mathrm{K}_t = \frac{{D_h}^2}{32} \qquad \text{(a7)}$$

This implies that the value of *c'* is 64.

When converting ducts with arbitrary rectangular cross-section to virtual ducts with circular cross-section, friction constants reported in the literature [29] for rectangular ducts with different width/length ratio, α, were divided by *c'* to obtain *c* as listed in Table 3. These values can be fitted with a polynomial (coefficient of correlation R^2=1):

$$c = 1.5 - 2.0364\alpha + 2.964\alpha^2 - 2.724\alpha^3 + 1.677\alpha^4 - 0.491\alpha^5 \qquad \text{(a8)}$$

According to Eq. a8, the value of *c* can be obtained for calculation of K_g for arbitrary gap length and width ratios, as demonstrated for the seven fabrics in Table 3.

References

[1] Mallick PK. Fiber-reinforced composites: materials, manufacturing, and design. Third Edition, Taylor & Francis Group, 2007.

[2] Krukenberg T, Paton R. Resin transfer molding for aerospace structures. Kluwer Academic Publishers, Netherlands, 1999.

[3] Long A. Design and manufacture of textile composites. Woodhead Publishing Limited, Cambridge, UK, 2005.

[4] Greene DL. Energy-efficiency improvement potential of commercial aircraft. Annual Review of Energy and Environment, 1992, 17: 537-573.

[5] Zeng X, Brown LP, Endruweit A, Matveev M, Long AC. Geometrical modelling of 3D woven reinforcements for polymer composites: Prediction of fabric permeability and composite mechanical properties. Composites Part A: Applied Science and Manufacturing, 2014, 56, 150-160.

[6] Hickey CMD, Bickerton S. Cure kinetics and rheology characterization and modelling of ambient temperature curing epoxy resins for resin infusion/VARTM and wet layup application. Journal of Materials Science, 2013, 48(2): 690-701.

[7] Endruweit A, Glover P, Head K, Long AC. Mapping of the fluid distribution in impregnated reinforcement textiles using Magnetic Resonance Imaging: application and discussion. Composites. Part A: Applied Science and Manufacturing, 2011, 42(10), 1369-1379.

[8] Grujicic M, Chittajallu KM, Shawn W. Lattice Boltzmann method based computation of the permeability of the orthogonal plain-weave fabric preforms. Journal of Materials Science, 2006, 41(23): 7989-8000.

[9] Mei CC, Vernescu B. Homogenization methods for multiscale mechanics, 2010: Singapore; London; World Scientific. 330.

[10] Mogavero J, Advani SG. Experimental investigation of flow through multi-layered preforms. Polymer Composites, 1997, 18(5): 649-655.

[11] Endruweit A, Long AC. Analysis of compressibility and permeability of selected 3D woven reinforcements. Journal of Composite Materials, 2010, 44(24): 2833-2862.

[12] Desplentere F, Lomov SV, Woerdeman DL, Verpoest I, Wevers M and Bogdanovich A. Micro-CT characterization of variability in 3D textile architecture. Composites Science and Technology, 2005, 65(13): 1920-1930.

[13] Badel P, Vidal-Salle E, Maire E and Boisse P. Simulation and tomography analysis of textile composite reinforcement deformation at the mesoscopic scale. Composites Science and Technology, 2008, 68(12): 2433-2440.

[14] Mahadik Y, Brown KAR and Hallett SR. Characterization of 3D woven composite internal architecture and effect of compaction. Composites Part A-Applied Science and Manufacturing, 2010, 41(7): 872-880.

[15] Awal A, Ghosh SB, Sain M. Development and morphological characterization of wood pulp reinforced biocomposite fibers. Journal of Materials Science, 2009, 44(11): 2876-2881.

[16] Karahan M, Lomov SV, Bogdanovich AE, Mungalov D, Verpoest I. Internal geometry evaluation of non-crimp 3D orthogonal woven carbon fabric composite. Composites Part A: Applied Science and Manufacturing, 2010, 41(9): 1301-1311.

[17] Rocha RPA, Cruz ME. Calculation of the permeability and apparent permeability of three-dimensional porous media. Transport in Porous Media, 2010, 83(2): 349-373.

[18] Gebart BR. Permeability of unidirectional reinforcements for RTM. Journal of Composites Materials, 1992, 26(8): 1101-1133.

[19] Cai Z, Berdichevesky AL. An improved self-consistent method for estimating the permeability of a fiber assembly. Polymer Composites, 1993, 14(4): 314-323.

[20] Bruschke MV, Advani SG. Flow of generalized Newtonian fluids across a periodic array of cylinders. Journal of Rheology, 1993, 37(3): 479-497.

[21] Xiao X, Long A, Zeng X. Through-thickness permeability modelling of woven fabric under out-of-plane deformation. Journal of Materials Science, 2014, 49: 7563-7574.

[22] Xiao X, Zeng X, Long AC, Cliford MJ, Lin H, Saldaeva E. An analytical model for through-thickness permeability of woven fabric. Textile Research Journal, 2012, 82(5): 492-501.

[23] Zupin Z, Hladnik A and Dimitrovski K. Prediction of one-layer woven fabrics air permeability using porosity parameters. Textile Research Journal, 2012, 82(2): 117-128.

[24] Mehaute B. An introduction to hydrodynamics & water waves. Springer-Verlag, New York, 1976.

[25] Sutera, SP, Skalak R. The history of Poiseuille's law. Annual Review of Fluid Mechanics, 1993. 25: 1-19.

[26] Advani SG, Bruschke MV, Parnas RS. Resin transfer molding flow phenomena in polymeric composites, In 'Flow and rheology in polymer composites manufacturing'. Elsevier science B. V, Amsterdam, 1994.

[27] Schlichting H., Gersten K. Boundary-Layer Theory. 8th Edition, Birlin, Hong Kong, Springer, c2000.

[28] Batchelor G.K. An introduction to fluid dynamics. Cambridge, Cambridge University Press, c1967.

[29] Papautsky I., Gale B.K., Mohanty S., Ameel T.A., Frazier A.B. Effects of rectangular microchannel aspect ratio on laminar friction constant. Proceedings of the Society of Photo-Optical Instrumentation Engineers (SPIE), 1999, 3877, 147-158

Table 1 Fabric specifications of seven woven fabric samples in average values (*Unit: 10^{-3} m*)

Fabric	Structure	R_f	Yarn V_f	L	λ	Yarn spacing		Yarn width	
						S_j	S_w	D_j	D_w
P_1	Plain	0.0043	0.56	0.323	5.23	0.470	0.410	0.405	0.279
T_1	2/1twill	0.0059	0.56	0.419	3.81	0.340	0.480	0.310	0.310
T_2	2/2twill	0.0057	0.56	0.610	4.10	0.342	0.446	0.313	0.380

			Fibre bundles		Inter-bundle voids	
			width	*height*	*width*	*height*
A_1	*N'*=1, L=2, V_F=0.41, λ=0.5	Warp	4.01 ±0.19	0.41 ±0.03	0.97 ±0.12	0.31 ±0.06
		Weft	3.16 ±0.19	0.38 ±0.04	0.49 ±0.20	0.34 ±0.04
		Binder	B_w 1.40 ±0.16	B_j 0.37 ±0.07		
A_2	*N'*=2, L=3.5, V_F=0.47, λ=0.5	Warp	4.02 ±0.21	0.42 ±0.05	0.83 ±0.15	0.23 ±0.05
		Weft	3.29 ±0.20	0.45 ±0.07	0.42 ±0.20	0.30 ±0.05
		Binder	B_w 1.48 ±0.16	B_j 0.35 ±0.04		
O_1	*N'*=1, L=5, V_F=0.55, λ=2.5	Warp	1.81 ±0.06	0.38 ±0.02	0.31 ±0.05	0.38 ±0.02
		Weft	2.07 ±0.12	0.35 ±0.03	0.32 ±0.07	0.35 ±0.03
		Binder	B_w 0.62 ±0.06	B_j 0.15 ±0.03		
O_2	*N'*=1, L=4.6, V_F=0.59, λ=2.5	Warp	1.77 ±0.08	0.40 ±0.03	0.29 ±0.04	0.40 ±0.03
		Weft	2.06 ±0.11	0.32 ±0.02	0.27 ±0.07	0.32 ±0.07
		Binder	B_w 0.73 ±0.17	0.15 B_j±0.06		

Table 2 Measured conversion ratios for one-layer woven fabrics and corresponding c values

Fabric	Width/length (α) of rectangular gap	*c* value
P_1	0.496	0.973
T_1	0.176	1.220
T_2	0.439	1.001
A_1	0.878	0.893
A_2	0.900	0.892
O_1	0.857	0.894
O_2	0.827	0.897

Rectangular gap width/length (α)	0.1	0.167	0.25	0.4	0.5	0.75	1
c value	1.323	1.231	1.140	1.023	0.972	0.905	0.889

Table 3 Comparison of the predicted yarn and inter-yarn gap permeabilities for one-layer woven fabrics

Fabric	Φ	Mean K_y *(Eq.19)* 10^{-13} m^2	Mean K_g *(Eq.18)* 10^{-10} m^2	Mean K_f *(Eq.12)* 10^{-12} m^2	$(1-\Phi)K_y/K_f$	$\Phi K_g/K_f$
P_1	3.93%	3.00	3.99	15.97	1.80%	98.20%
T_1	1.64%	4.98	2.19	4.08	12.01%	87.99%
T_2	1.08%	3.13	2.63	3.14	9.86%	90.14%

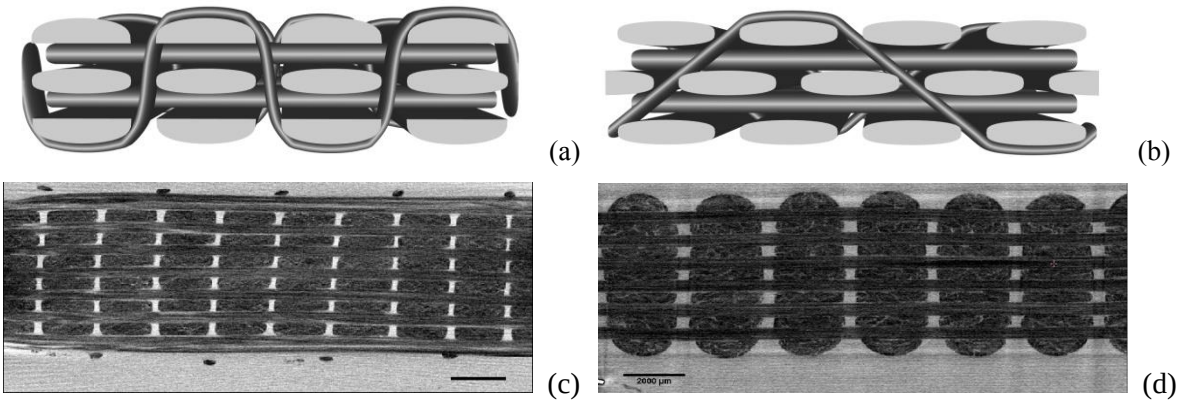

Fig.1 Simulated cross-sections of **a** orthogonal and **b** angle-interlock woven fabrics, and real cross-sections of an orthogonal fabric (**c**, **d**) obtained by X-ray micro-*CT* scanning [14]

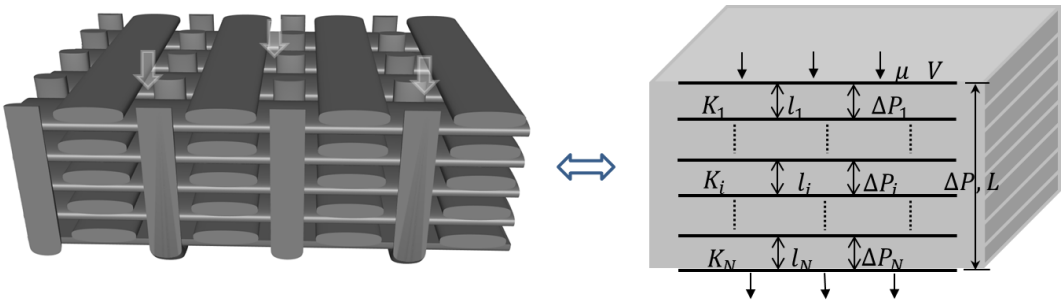

Fig.2 Schematic of fluid flow through a 3D-woven fabric

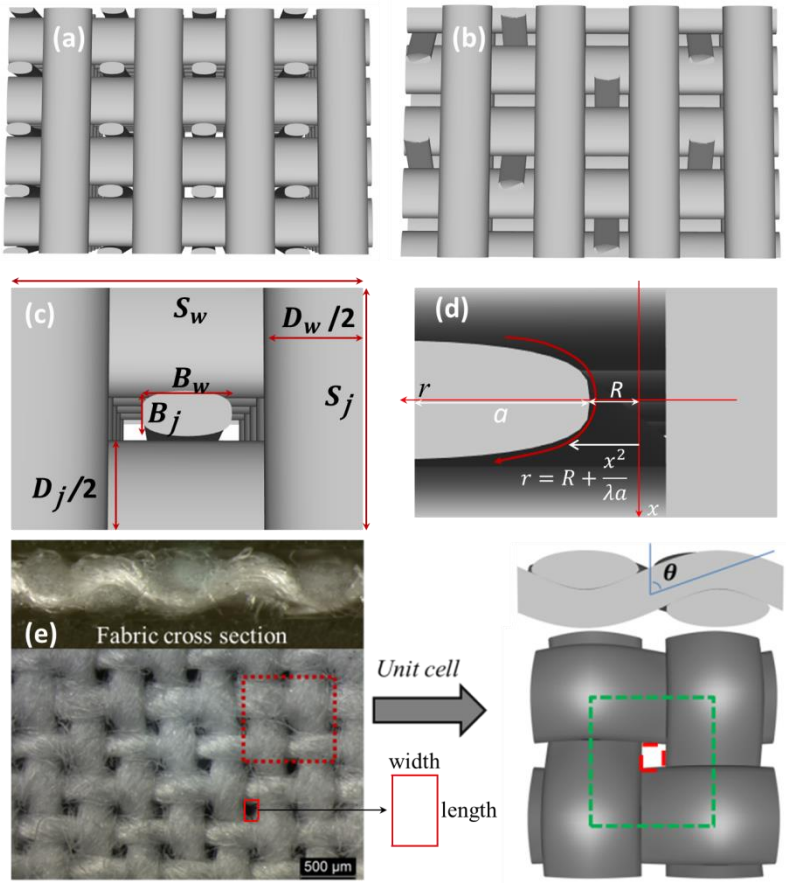

Fig.3 Top view of **a** orthogonal **b** angle-interlock woven fabrics; **c** top view of a unit-cell of orthogonal and **d** lateral view of a warp/weft with dimensions; **e** Left: top and lateral views of a plain woven fabric structure; Right: a fabric unit-cell where the red frame represents the inter-yarn gap and the green frame represents the yarn area, θ is the yarn crimp angle

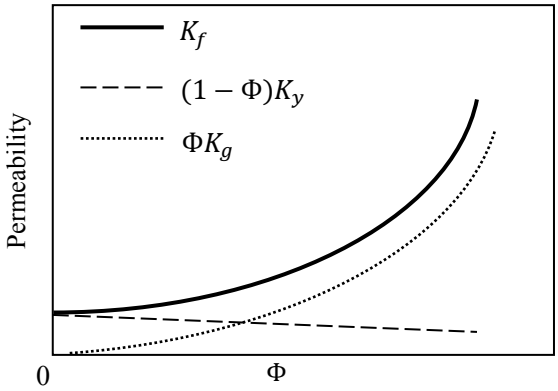

Fig.4 Schematic of relationship of three permeabilities: K_y, K_g and K_f

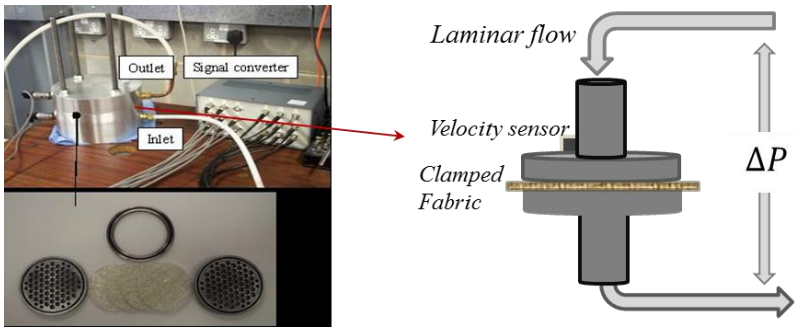

Fig.5 Permeability tester and schematic of the instrument working principle

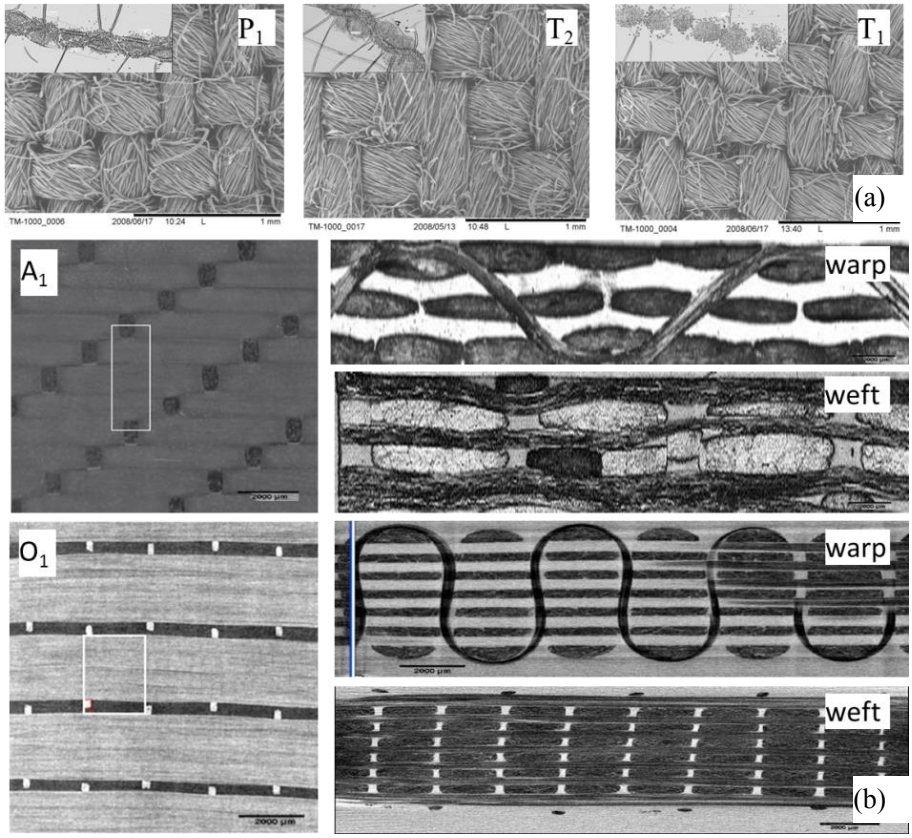

Fig.6 a top and cross-section views of woven fabrics P_1, T_1, T_2; **b** top, along warp and weft cross-section views of fabrics A_1 and O_1

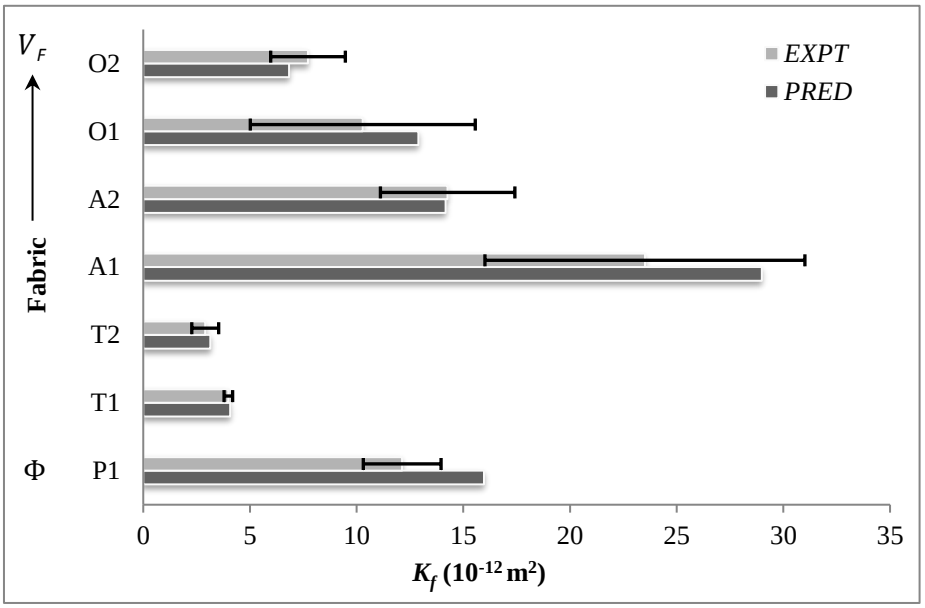

Fig.7 Prediction of fabric permeability (Eqs.8, 12, 18 & 20) compared against experimental data